Omnidirectional Wireless Power Transfer System Using Modified Saddle-Shaped Coil Pair for Implantable Capsule Robots

Haoyu Zhuang, Wei Wang, and Guozheng Yan

***Abstract*—Wireless power transfer (WPT) technology has been widely researched and developed, especially the omnidirectional WPT system. Despite much attention, the omnidirectional WPT system generating 3-D magnetic field is rarely reported for capsule robot (CR) applications. In this article, we propose a genuine omnidirectional system for CR using only one pair of power transmitting coils (PTCs) and one power receiving coil (PRC) for the first time. The novel PTC with a compact and compatible structure is capable of generating 3-D magnetic field at any position. In particular, a single power source is solely utilized to drive the PTC without current amplitude or phase control methods. Based on the magnetic calculation and finite-element simulation, the geometric parameters of the proposed PTC structure are determined. Additionally, through the theoretical analysis and comparison with traditional topology, the capability of omnidirectional transfer can be verified. Furthermore, in order to dynamically adjust the PTC rotation, the corresponding received voltage tracking-based control strategy is also illustrated. Finally, a practical prototype is built, and experimental results confirm the omnidirectional WPT capability of the proposed system concerning both positions and attitudes, as well as the effectiveness of the control method. It demonstrates a maximum power delivered to the load of 2523 mW with a power transfer efficiency of 8.4%.**

***Index Terms*—Capsule robot, omnidirectional system, power transfer efficiency, power transmitting coil, wireless power transfer.**

I. Introduction

THE development of wireless power transfer (WPT) technology offers a potential solution for power supply and brings new vitality to the areas of electric vehicles [1], implantable medical devices (IMDs) [2], robotics [3], portable electronics [4], etc. However, unlike the other applications, the WPT for IMDs, especially the capsule robots (CRs), faces additional design challenges:

1) The attitude of the CR is unpredictable due to the irregular gastrointestinal tract, which requires the WPT system to be omnidirectional in 3-D space.
2) The position of the CR is unpredictable, which necessitates the uniform magnetic field covering all the working space of the CR.
3) The power transfer efficiency (PTE) is generally low owing to the huge difference in coil size as well as the misalignment between the power transmitting coil (PTC) and power receiving coil (PRC).
4) The human exposure safety must be ensured.

Considerable efforts have been put in to design omnidirectional WPT systems, which eliminates blind spots in 2-D and 3-D spaces. Among them, orthogonal structures composed of three orthogonal round coils are widely used in omnidirectional WPT systems due to simple structure and theoretically no mutual inductance [5], [6], [7], [8], [9], [10]. Employing the nonidentical current method to generate rotating magnetic field vector in a truly omnidirectional manner is analyzed both for 2-D [5] and 3-D [6]. However, despite its good omnidirectional performance, three independent power supplies are irreducible because multiple coils connected in series can only generate the power flow in a resultant direction of the vector sum [11], and the corresponding control methods, namely frequency modulation, phase difference, or current amplitude control, are also complicated [7]. Crossed dipole coils with ferromagnetic cores inserted are also proposed as another form to generate rotating magnetic field based on phase difference control, whereas the structure is more flexible compared with the orthogonal coils [12]. The common limitation of these rotating magnetic field configurations is the inefficient power as most of the magnetic flux is not picked up by the target load. For this reason, the rotating magnetic field method is more suitable for the scenario of multiple receivers [9]. Then, the WPT system using only a single power source to drive the stereoscopic cubic transmitter is proposed [13], while the omnidirectional power transfer capability is simply verified for the outer 2-D cylindrical surface. Other approaches have been reported utilizing multiple PTCs such as the combination of a birdcage coil and a Helmholtz coil [14], bowl-shaped coils [15], and planar coils array [16] to eliminate the impact of positional misalignment. It has been pointed out that for the genuine

Manuscript received 21 March 2023; accepted 22 April 2023. Date of publication 27 April 2023; date of current version 28 July 2023. This work was supported in part by the National Natural Science Foundation of China under Grants 81971767, 62103263, and 62103267, in part by the Projects of Science and Technology Commission of Shanghai Municipality under Grants 19142203800, 19441913800, 19441910600, and 21ZR1429900, in part by the National Facility for Translational Medicine (Shanghai) Open Project Fund under Grant TMSK-2021-302, and in part by the Shanghai Pujiang Program under Grant 20PJ1419300. Recommended for publication by Associate Editor A. Kuperman. *(Corresponding author: Guozheng Yan.)*

The authors are with the Department of Instrument Science and Engineering, Shanghai Jiao Tong University, Shanghai 200240, China (e-mail: divine_zhy@sjtu.edu.cn; aries-wang@sjtu.edu.cn; gzhyan@sjtu.edu.cn).

Color versions of one or more figures in this article are available at https://doi.org/10.1109/TPEL.2023.3270501.

Digital Object Identifier 10.1109/TPEL.2023.3270501

omnidirectional WPT, the currents should be nonidentical so that the load can pick up rotating magnetic field vectors in all directions [7]. Therefore, some of the methods mentioned above are not strictly omnidirectional WPT since the direction of the magnetic field at a certain position cannot be changed.

In order to realize the genuine omnidirectional WPT, it is necessary to satisfy $m_{\mathrm{t}} + m_{\mathrm{r}} \geq 4$, where m_{t} and m_{r} denotes the number of PTCs and PRCs, respectively [12]. As for the WPT system for CR, the particularity lies in that the design of PTC should take into account the applicability of accommodating human body. Therefore, the above-mentioned *in vitro* multidimensional PTC structures are generally not suitable for CRs, and consequently many efforts concentrate on the 3-D PRC design with $m_{\mathrm{t}} = 1$ and $m_{\mathrm{r}} = 3$, to realize the omnidirectional power pickup [17], [18], [19], [20], [21]. In general, ferrite cores are inserted to enhance the coupling, and the 3-D PRCs can be coin-type [17], tube-type [18], [19], cubic-type [20], and cross-type [21]. However, all types occupy too much space in CRs compared with the 1-D ones [22], [23], [24]. So far, no genuine omnidirectional WPT system with 3-D PTC designed for CRs has been reported.

To overcome these limitations, in this article, a genuine omnidirectional WPT system for CRs using only one pair of PTCs and one PRC is proposed for the first time. Moreover, we also propose the received voltage tracking-based control strategy (RVTCS) to dynamically adjust the rotation angle of the PTC, hence ensuring the stability and continuity of received power regardless of the attitudes of PRCs. The proposed system has the following advantages:

1) Genuine omnidirectional system, which means the PRC can pick up sufficient power with any attitude at any position.
2) Compact and compatible structure for CR application adopting only one pair of PTCs and one PRC, and hence releasing the limited inner space of CR for more functional modules.
3) Designed for single target device, and avoiding the power waste caused by the lack of concentration of magnetic field vectors compared with the rotating magnetic field mode.
4) Only a single power source is needed as well as the simple control.

The rest of this article is organized as follows. Section II presents the omnidirectional WPT system proposed for the CRs. In Section III, the novel PTC structure of translational misaligned saddle-shaped coil pair is proposed. Then, the geometric parameters are determined based on the magnetic calculation and finite-element simulation optimization. The omnidirectional transmission capability of the 1-D PTC generating 3-D magnetic field is analyzed and compared with the traditional topology of 3-D PRC in 1-D magnetic field in Section IV. In addition, the corresponding received voltage tracking-based control strategy is also proposed and illustrated. In Section V, prototype of the proposed omnidirectional WPT system is established and tested through experiments to validate the omnidirectional performance as well as the control strategy. Finally, conclusions are given in Section VI.

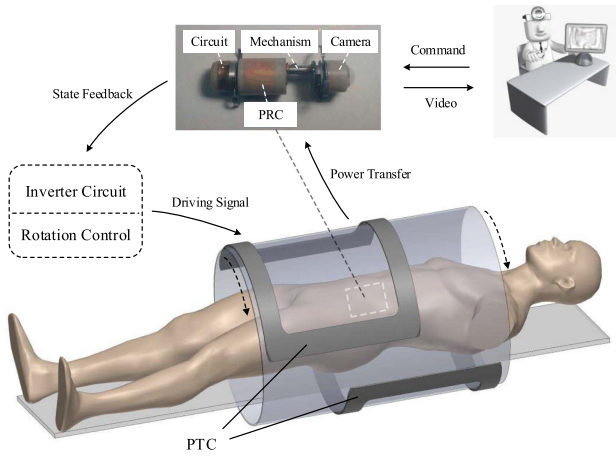

Fig. 1. Schematic diagram of the proposed WPT system for CRs.

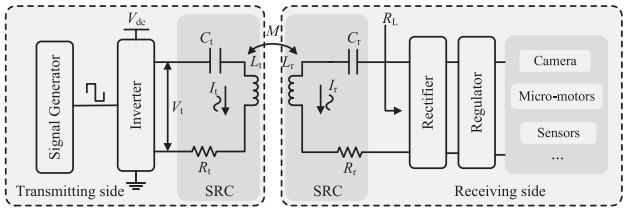

Fig. 2. Equivalent circuit model of the WPT system for CRs.

II. WPT System for CR

Fig. 1 shows the schematic diagram of the proposed WPT system for CRs while Fig. 2 displays the equivalent circuit model. In the typical WPT system based on magnetic resonant coupling, the alternating magnetic field generated by the PTC on the transmitting side and driven by the external inverter and control circuit is picked up by the PRC embedded in the CR on the receiving side. Through the full-bridge rectification and low drop-out linear regulator, the continuous dc voltage can be used by CRs to complete the locomotion and diagnosis. Both the transmitting side and receiving side adopts the series resonant circuit (SRC) to achieve the resonance as the series–series topology is the only one topology, that is independent on the coupling coefficient and the load condition [25]. To make the circuits tune at a specific transmission frequency f $(= \omega/2\pi)$ different from the intrinsic frequency of coils, the compensation capacitors C_{t} and C_{r} are connected in series. M represents the mutual inductance between inductance L_{t} and L_{r}. R_{t}, R_{r}, and R_{L} represent the equivalent series resistances of PTC, PRC, and load, respectively. The PTE can be calculated as [26]

$$\eta = \frac{P_{\mathrm{L}}}{P_{\mathrm{t}}} = \frac{I_{\mathrm{r}}^2 R_{\mathrm{L}}}{I_{\mathrm{t}} V_{\mathrm{t}}} = \frac{\omega^2 M^2 R_{\mathrm{L}}}{R_{\mathrm{t}} \left(R_{\mathrm{r}} + R_{\mathrm{L}}\right)^2}. \tag{1}$$

The huge difference between the size of PTC and PRC as well as the uncertainty of PRC position and attitude results in loose coupling. Hence, the PTE is generally low. To address the loose coupling and low PTE, the capability of 3-D omnidirectional WPT is indispensable. However, the PTC configuration of a

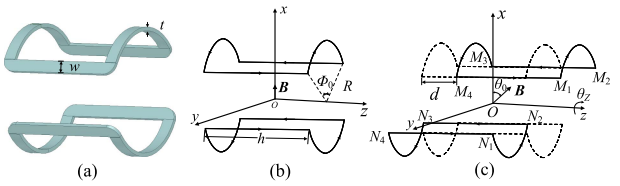

Fig. 3. Schematic diagram of (a) the traditional SCP, (b) the simplified wireframe, and (c) the proposed TMSCP.

single coil pair can only generate magnetic field at a fixed direction. Herein, the original 1-D PTC is designed to have a asymmetric structure with axial misalignment, thus generating a magnetic field vector with an inclination angle relative to the central axis. With the controllable rotation around the central axis, the 1-D magnetic field can cover the 3-D space to ensure adequate components in any direction.

III. PTC Design and Parameters Optimization

A. Translational Misaligned Saddle-Shaped Coil Pair

Typically, saddle-shaped coil pairs (SCPs) are widely used in applications requiring uniform magnetic fields, e.g., magnetic resonance imaging, nuclear magnetic resonance spectrometer, atomic magnetometers, and atomic gyros [27], [28]. In these cases, the space available for the coil system is limited and of cylindrical symmetry. Notably, the uniformity of magnetic field is highly sensitive to the geometrical parameters, which should be chiefly considered [27].

The schematic diagram of the traditional SCP is illustrated in Fig. 3(a) while Fig. 3(b) shows the simplified wireframe. The typical SCP form consists of two identical rectangular planar coils confined to a cylindrical surface with axial height h, radius of the cylinder R, coil width w, and thickness t. ϕ_0 denotes the central angle. Apparently, the cylindrical structure is space-saving and fully compatible with the CR application to allow a patient to lie in. The proposed translational misaligned saddle-shaped coil pair (TMSCP) is shown in Fig. 3(c). Both coils are axially translated in opposite directions by a distance of d with respect to the original position. Besides, the PTC is designed to be able to pivot around z-axis with an angle of θ_Z.

The length-to-diameter ratio $\alpha\ (=h/2R)$ and central angle ϕ_0 are the determining factors in terms of the magnetic field uniformity. α of 2 and ϕ_0 of 120° is the ideal configuration for the typical SCP, which is obtained by cancelling the second-order derivatives of the central field in any direction [29]. However, only the local magnetic field uniformity within a small space volume around the central point is focused in [29]. Moreover, after the translation, the centers of the two coils are no longer aligned and are separated by $2d$. Hence, the conclusions concerning magnetic field uniformity of traditional SCP need to be reconsidered herein.

B. Magnetic Field Calculation

The magnetic flux density expression of the proposed TMSCP at the origin can be calculated by accumulating the contributions of each arc and line segment using the Biot–Savart law. Noting that the TMSCP is symmetrical about xoz plane, the y component is zero and thus free from being calculated. To be specific, the magnetic flux density generated by the arcs, namely M_1M_2, M_3M_4, N_1N_2, and N_3N_4, can be obtained as

$$\begin{cases} B_{x,\,\text{arc}} = \dfrac{\mu_0\, NI}{2\pi} \sin\dfrac{\phi_0}{2} \cdot \left(\dfrac{R(h+2\,d)}{[(d+h/2)^2+R^2]^{\frac{3}{2}}} + \dfrac{R(h-2\,d)}{[(h/2-d)^2+R^2]^{\frac{3}{2}}} \right) \\ B_{z,\,\text{arc}} = \dfrac{\mu_0\, NI\phi_0}{2\pi} \left(\dfrac{-R^2}{[(d+h/2)^2+R^2]^{\frac{3}{2}}} + \dfrac{R^2}{[(h/2-d)^2+R^2]^{\frac{3}{2}}} \right) \end{cases} \tag{2}$$

where N is the number of turns, I is the current, and μ_0 is the permeability of free space. As for the line segments M_2M_3, M_4M_1, N_2N_3, and N_4N_1, the magnetic flux density has no z component, and the x component is as follows:

$$B_{x,\,\text{line}} = \frac{\mu_0\, NI}{\pi R} \sin\frac{\phi_0}{2} \cdot \left(\frac{d+h/2}{[R^2+(d+h/2)^2]^{\frac{1}{2}}} + \frac{h/2-d}{[R^2+(h/2-d)^2]^{\frac{1}{2}}} \right). \tag{3}$$

Thus, the total magnetic flux density B_{TMSCP} can be written as

$$\begin{cases} B_{x,\text{TMSCP}} = \dfrac{\mu_0\, NI}{\pi R} \sin\dfrac{\phi_0}{2} \cdot \left(\dfrac{R^2C_1}{\left(C_1^2+R^2\right)^{\frac{3}{2}}} + \dfrac{R^2C_2}{\left(C_2^2+R^2\right)^{\frac{3}{2}}} + \dfrac{C_1}{\left(C_1^2+R^2\right)^{\frac{1}{2}}} + \dfrac{C_2}{\left(C_2^2+R^2\right)^{\frac{1}{2}}} \right) \\ B_{z,\text{TMSCP}} = \dfrac{\mu_0\, NI\phi_0}{2\pi} \left(\dfrac{-R^2}{\left(C_1^2+R^2\right)^{\frac{3}{2}}} + \dfrac{R^2}{\left(C_2^2+R^2\right)^{\frac{3}{2}}} \right) \end{cases} \tag{4}$$

where $C_1 = h/2 + d$ and $C_2 = h/2 - d$.

Though the central magnetic flux density is computable, the expression of magnetic flux density in free space apart from the origin, as well as the analytical method using Taylor series expansions [27], has become complex and tedious as the symmetry is not applicable and additional variables are introduced. Furthermore, the deviations caused by the approximate simplification of the coil width are not considered. Therefore, another method of finite-element analysis (FEA) is adopted in this article to obtain more intuitive results.

C. Finite Element Analysis

Noting that in most cases, a large coil height, i.e., a large α, generally cannot be satisfied due to the experimental restrictions. Considering the tradeoff between the length-to-diameter ratio restriction and the magnetic field uniformity, compromised values of $\alpha = 0.75$, 1, and 1.25 are chosen and compared in the following analysis. In this case, the corresponding optimal central angles can be determined as 130.4°, 124.3°, and 121.6° to maximize the uniformity of the main magnetic field component [27]. Due to the symmetry of the typical SCP, we know that

TABLE I
CALCULATED AND SIMULATED RESULTS OF DIFFERENT CONFIGURATIONS OF PTC PARAMETERS

α	h (mm)	ϕ_0 (°)	Calculated d (mm)	Simulated d (mm)	$B\|_{(0,0,0)}$ (T)	γ	$\Delta\theta$ (°)
0.75	300	144.1	149.3	148	5.49×10^{-5}	82.5	5.35
1	400	130.4	193.9	191	5.43×10^{-5}	85.4	4.26
1.25	500	124.3	240.2	236	5.38×10^{-5}	86.0	3.53

the magnetic flux density has no y or z components at the origin. For the proposed TMSCP in this article, in order to generate a magnetic flux density vector projecting equal components in x and z directions, z component can be obtained with the introduction of d according to (4). Ideally, the value of the angle θ_0 formed with the positive direction of x axis is 45° at the origin. Thus, the distance d can be calculated by making $B_{x,\text{TMSCP}}$ and $B_{z,\text{TMSCP}}$ equal. The results of the calculated d using MATLAB can be found in Table I. Additionally, the simulated d is also obtained with the help of ANSYS Maxwell to make a comparison. It can be found that the calculated results of d are highly consistent with the simulated results, and the main reason for the slight difference is that the theoretical solution does not take into account the actual coil width. A cubic space with a side length of 100 mm centered on the origin is employed to evaluate the uniformity. To intuitively quantify the relative uniformity in amplitude within the sample space, parameter γ is defined as

$$\gamma = \left(1 - \frac{(B_{\max} - B_{\min})}{B|_{(0,0,0)}}\right) \times 100\% \tag{5}$$

and the uniformity in magnetic flux density direction is evaluated by the maximum angular deviation of the magnetic flux density direction between the points in space and the origin. From the results in Table I, we can see that with the decrease of α, the magnetic flux density shows an insignificant increase while uniformity declines. However, although the three configurations differ greatly in axial overall length l_{total} $(= h + 2d)$, the slight difference in uniformity can be negligible. Therefore, in order to make the structure compact and lightweight, the configuration of $\alpha = 0.75$ is more reasonable and hence adopted in this article.

Once the geometric parameters are determined, the variation of d affects the magnetic field directions and the distribution of magnetic flux density. To better illustrate it, Fig. 4 shows the magnetic flux density in the plane $x = -40$ mm, 0 mm, and $+40$ mm with four different d as 0 mm, 98 mm, 148 mm, and 196 mm, and the corresponding θ_0 is 0°, 30°, 45°, and 60°, respectively. The distribution of the magnetic flux density in yoz plane, i.e., $x = 0$ mm, is centrosymmetric about the origin due to the symmetry of the PTC geometric structure, whereas the magnetic flux density at other positions in space tends to be asymmetric and shifts to one side with the increase of d. It also reveals from Fig. 4 that the directions of the magnetic flux density in the cubic space, which are marked with arrows, are basically consistent. Thus, it ensures that the angle corresponding to the maximization of magnetic flux is almost the same at any position, which makes the omnidirectional WPT controllable.

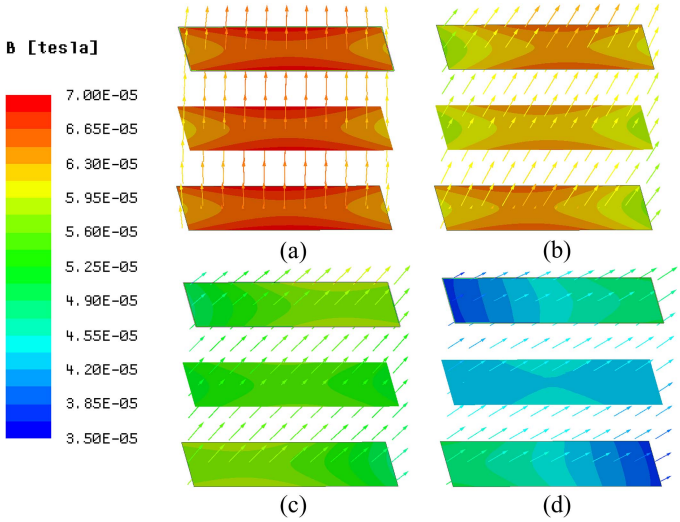

Fig. 4. Magnetic flux density in the plane $x = -40$ mm, 0 mm, and $+40$ mm with d of (a) 0 mm, (b) 98 mm, (c) 148 mm, and (d) 196 mm.

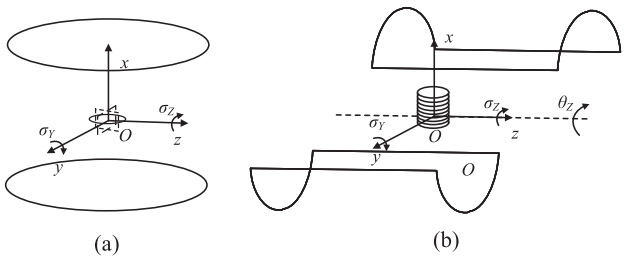

Fig. 5. Topology of (a) 3-D PRC in 1-D magnetic field and (b) 1-D PRC in 3-D magnetic field.

IV. OMNIDIRECTIONAL TRANSMISSION

A. Theoretical Analysis

To better illustrate the omnidirectional transmission capability, the proposed topology is analyzed theoretically and compared with the traditional omnidirectional topology with 3-D PRC. Fig. 5 depicts schematic diagrams of the two different WPT topologies. As shown in Fig. 5(a), the traditional 3-D PRC is generally used when the external magnetic field is only 1-D. It is composed of three independent PRCs, which are perpendicular to each other and connected in parallel or in series after rectification. σ_Y is the angle of the PRC pivoting around y-axis, and σ_Z is the angle pivoting around z-axis. It should be noted that σ_Y is always rotated before σ_Z. Due to symmetry, σ_Y and σ_Z are limited to $0 \le \sigma_Y < \pi$ and $0 \le \sigma_Z < 2\pi$. Fig. 5(a) and (b) displays the attitude of the PRCs when $\sigma_Y = \sigma_Z = 0°$. When sinusoidal driving current $I_t = I_m \sin(2\pi f t)$ is generated in the transmitting side, the root-mean-square induced electromotive force (EMF) of PRC i $(i = a, b, c)$ can be written as

$$\varepsilon^i_{\text{rms}} = \sqrt{2}\pi f I_m M^i_0 g_i \quad (i = a, b, c), \tag{6}$$

where M^i_0 represents the mutual inductance between PRC i and PTC when the enclosed plane of PRC i is exactly vertical to the magnetic field generated by the PTC, and g_i represents the

attitude factors of PRC i ($0 \le g_i \le 1$). Assuming that $M_0^a = M_0^b = M_0^c = M_0$, which is the ideal configuration, and the three PRCs are connected in series, the total root-mean-square induced EMF ε_{rms} can be obtained as

$$\varepsilon_{\text{rms}} = \varepsilon_0 \left(|\cos\sigma_Y \cos\sigma_Z| + |\sin\sigma_Y \cos\sigma_Z| + |\sin\sigma_Z|\right) \quad (7)$$

where $\varepsilon_0 = \sqrt{2}\pi f I_{\text{m}} M_0$. Thus, the ratio of the maximum to the minimum of ε_{rms} can be obtained as $\sqrt{3}$, which is also verified in [30] as well as the determination of connection way in [31].

For the WPT system proposed in this article shown in Fig. 5(b), which utilizes the rotatable TMSCP with a pivoting angle $\theta_Z (0 \le \theta_Z < 2\pi)$ around z-axis as the 3-D magnetic field generator and the space-saving 1-D PRC replacing the traditional 3-D PRC, the root-mean-square induced EMF $\varepsilon'_{\text{rms}}$ can be calculated as

$$\varepsilon'_{\text{rms}} = \varepsilon'_0 \left|\cos\theta_{\text{d}}\right| \quad (8)$$

where $\varepsilon'_0 = \sqrt{2}\pi f I_m M'_0$, and M'_0 represents the mutual inductance between the 1-D PRC and the proposed omnidirectional PTC when the enclosed plane of PRC is exactly vertical to the magnetic field generated by the PTC, and θ_{d} represents the angle between the normal direction of the enclosed plane of the 1-D PRC and the direction of the magnetic field. The unit direction vector of the magnetic field generated by the rotatable TMSCP can be represented as

$$\boldsymbol{v}_{\text{t}} = \frac{\sqrt{2}}{2}\cos\theta_Z \boldsymbol{i} - \frac{\sqrt{2}}{2}\sin\theta_Z \boldsymbol{j} + \frac{\sqrt{2}}{2}\boldsymbol{k} \quad (9)$$

where $\boldsymbol{i}$, $\boldsymbol{j}$, $\boldsymbol{k}$ represents the unit vector of x, y, and z axis, respectively. The unit direction vector of the 1-D PRC can be represented as

$$\boldsymbol{v}_{\mathbf{r}} = \cos\sigma_Y \cos\sigma_Z \boldsymbol{i} - \cos\sigma_Y \sin\sigma_Z \boldsymbol{j} + \sin\sigma_Y \boldsymbol{k}. \quad (10)$$

Thus,

$$\begin{aligned}\cos\theta_{\text{d}} &= \frac{\sqrt{2}}{2}\left(\cos\theta_Z \cos\sigma_Y \cos\sigma_Z + \sin\sigma_Y \right.\\ &\quad \left. + \sin\theta_Z \cos\sigma_Y \sin\sigma_Z\right)\\ &= \frac{\sqrt{2}}{2}\left(\cos\sigma_Y \cos\left(\theta_Z - \sigma_Z\right) + \sin\sigma_Y\right). \end{aligned} \quad (11)$$

Clearly, (8) and (11) indicate that the range of $\varepsilon'_{\text{rms}}$ depends on how well θ_Z follows σ_Z, i.e., the differential value between θ_Z and σ_Z. A special case is that if

$$\begin{cases}\theta_Z = \sigma_Z, & 0 \le \sigma_Y < \frac{\pi}{2}\\ \theta_Z = \sigma_Z + \pi, & \frac{\pi}{2} \le \sigma_Y < \pi\end{cases} \quad (12)$$

is satisfied

$$\cos\theta_{\text{d}} = \begin{cases}\sin\left(\sigma_Y + \frac{\pi}{4}\right), & 0 \le \sigma_Y < \frac{\pi}{2}\\ \sin\left(\sigma_Y - \frac{\pi}{4}\right), & \frac{\pi}{2} \le \sigma_Y < \pi\end{cases} \quad (13)$$

gets the maximum value when $\sigma_Y = \frac{\pi}{4}$ or $\frac{3\pi}{4}$, and the minimum value when $\sigma_Y = 0$ or $\frac{\pi}{2}$. Hence, the ratio of the maximum to the minimum of $\varepsilon'_{\text{rms}}$ can be obtained as $\sqrt{2}$, which shows a better angular uniformity compared with the configuration of 1-D PTC/3-D PRC. In short, when the attitude of PRC is given with an arbitrary σ_Y and σ_Z, the control strategy of θ_Z is crucial to the value of $\varepsilon'_{\text{rms}}$, and is further analyzed in detail in the following section.

B. Dynamic Control Strategy of θ_Z Based on Received Voltage Tracking

As mentioned above, θ_Z plays a decisive role in the root-mean-square induced EMF, and hence, we herein propose a received voltage tracking-based control strategy (RVTCS) to adjust θ_Z dynamically. The load received voltage V_{L} can be calculated as

$$V_{\text{L}} = \varepsilon'_{\text{rms}} \frac{R_{\text{L}}}{R_{\text{r}} + R_{\text{L}}}. \quad (14)$$

In order to maximize $\varepsilon'_{\text{rms}}$, as indicated in (11)–(13), θ_Z should closely follow the change of σ_Z. However, since the attitude of normally working CRs keep changing and unpredictable, it is difficult to guarantee (12) at all times. Moreover, V_{L} is allowed to fluctuate within a certain range due to the introduction of voltage regulator. Considering these factors, the lower voltage limit V_{Ls} should be slightly lower than the minimum load received voltage with $\theta_Z = \sigma_Z$ and $\sigma_Y = 0$, and the maximum load received voltage V_{Lm} is measured when $\theta_Z = \sigma_Z$ and $\sigma_Y = \frac{\pi}{4}$ according to (12)–(14). V_{Ls} is also the starting voltage threshold, which means when the load received voltage $V_{\text{L},t}$ at time t is insufficient and below the lower voltage limit due to the attitude change of CR, i.e., $V_{\text{L},t} < V_{\text{Ls}}$, the PTC starts to rotate positively or negatively and, hence, increase or decrease θ_Z so as to raise $V_{\text{L},t}$ and search for the peak value until $|V_{\text{L},t} - V_{\text{L},t-1}| < \Delta V_{\text{L}}$, where ΔV_{L} represents the acceptable voltage tolerance to terminate rotation. Undoubtedly, the peak load received voltage V_{Lp} at the random σ_Y and σ_Z is not exactly the same, whereas V_{Lp} must be higher than V_{Ls} and not exceeding V_{Lm}. If V_{L} drops below V_{Ls} as the attitude of CR is changed, the alignment process is repeated. In conclusion, the RVTCS can be summarized as the control flow in Fig. 6.

V. Experimental Verification

A. Experimental Setup

As shown in Fig. 7, the prototype of the proposed TMSCP is built with insulated acrylic frame and 180 strands of AWG 38 Litz wire to alleviate ac loss [32]. The angle of PTC rotation θ_Z is realized by the drive of servo motor. Specifically, under the control of PWM signal, which is generated by an Arduino board, the servo motor can easily rotate by a given angle or at a certain speed. The received voltage is measured by resistance sampling and processed by the onboard microcontroller PIC24F16KA102. The voltage data are then sent to the external Arduino board where RVTCS is implemented, through the wireless communication chips Si4455 (Silicon Labs) working at 433 MHz. The output shaft of the motor drives the transmission gear to mesh with the external gear ring on the outer wall of the acrylic coil frame, thus driving the PTC to rotate. A typical 1-D PRC is adopted here to evaluate the omnidirectional magnetic field generated by the proposed PTC. Enameled copper wire is tightly wound on the surface of hollow cylindrical ferrite core to concentrate the magnetic flux and enhance the coupling [22].

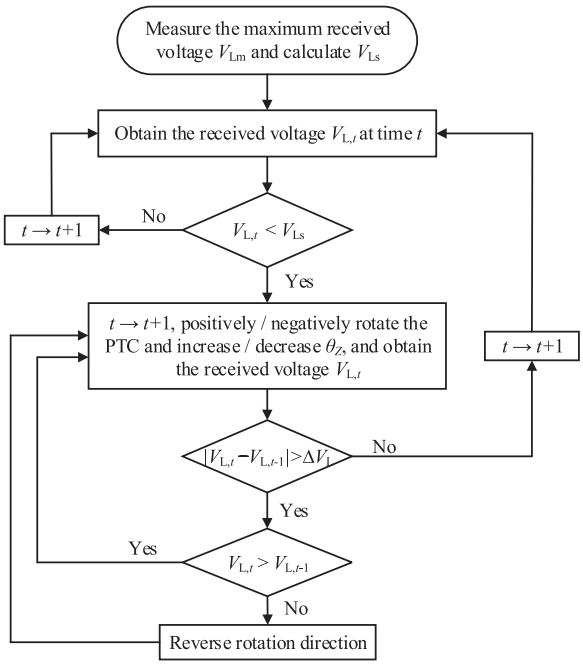

Fig. 6. Control flow of the proposed RVTCS.

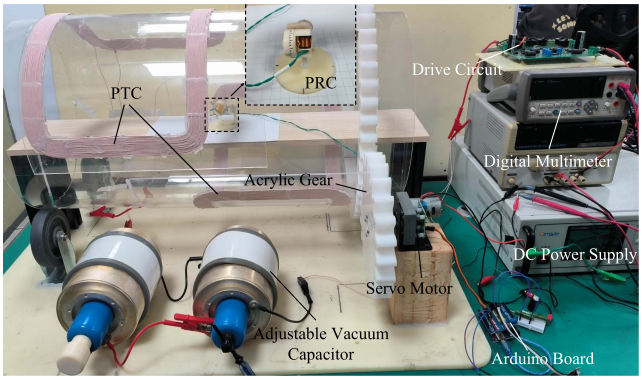

Fig. 7. Experimental setup of the proposed WPT system.

TABLE II
MAIN CHARACTERISTIC PARAMETERS OF THE FABRICATED PTC AND PRC

Parameter	PTC	PRC
Size	R: 200 mm, h: 300 mm, d: 148 mm	Φ13 mm × 9 mm
Turns number	20 × 2	75
Winding wire	180 strands of AWG 38 Litz wire	AWG 33 enameled copper wire
Ferrite core size and material	None	Φ(11-13) mm × 15 mm, R6K
Equivalent series resistance	2.1 Ω @ 218 kHz	8.41 Ω @ 218 kHz
Self-inductance	773.3 μH	282.9 μH
Quality factor	503.6	46

Table II lists the main characteristic parameters of the fabricated PTC and PRC. The resonant frequency is set to 218 kHz, which is verified for its performance and human tissue safety in [26], [33], and [34]. A 30-Ω load resistance is connected in series to simulate the equivalent load of the normally working CR [20], [22]. As a preliminary reference, the input power is set to be 30 W (12 V, 2.5 A) in the following tests.

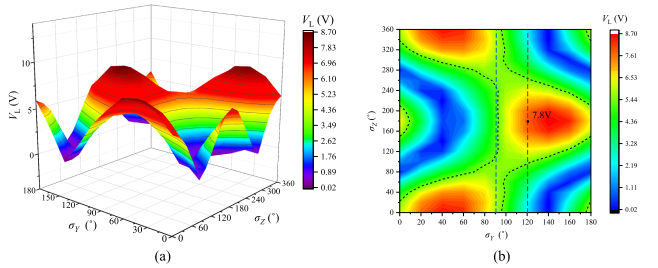

Fig. 8. Measured load received voltage V_L distribution at the origin versus different σ_Y and σ_Z. (a) 3-D surface graph and (b) 2-D projection drawing.

B. EMF Safety

Though the field attenuation in biological tissues is quite negligible at the employed frequency [35], [36], the EMF exposure should be assessed and limited in a safe range to avoid the human safety issues such as heating effects and nerve stimulation. According to the International Commission on Non-Ionizing Radiation Protection (ICNIRP) guidelines [37], [38], the basic restrictions (BRs) for human exposure to EMF at 218 kHz are given in terms of both the internal induced electric field E and the specific absorption rate (SAR). However, for the frequencies below 1−2 MHz, the influence of induced electric field E is proved to be dominant [26], [35]. A simplified human torso model [26], [39] composed of multilayer biological tissue is used to calculate the simulated E value. Under the given excitation, the calculated maximum E and SAR are 22.5 V/m and 0.64 W/kg, respectively, which are far below the specified BR standard for 218 kHz (29.43 V/m for E and 2 W/kg for SAR). The maximum allowed current is 3.3 A for the proposed configuration. Thus, the fixed 30 W input power can guarantee the human exposure safety.

C. Angular Distribution of Measured Received Voltage

To adjust the attitude of the PRC in a simple way, a three-axis rotatable test platform is designed and fabricated, as displayed in Fig. 8. With the platform, the tested PRC can conveniently pivot around a single axis or multiple axes by specific angles without position deviation thanks to the triaxial concentricity. For the sake of brevity, the combination of σ_Y, σ_Z, and θ_Z is abbreviated as (σ_Y, σ_Z, θ_Z) and expressed in degrees hereinafter. The rotatable platform is placed in the center of the PTC, namely the origin, and the PTC is fixed with a constant $\theta_Z = 0°$. The 3-D surface graph of the measured load received voltage V_L distribution at the origin versus different σ_Y and σ_Z ranging from (0°, 0°, 0°) to (180°, 360°, 0°) is shown in Fig. 8(a) as well as the 2-D projection drawing in Fig. 8(b). It can be intuitively found that the maximum value of V_L exists near (45°, 0°, 0°) and (135°, 180°, 0°), which accords with the results of (12) and (13), and the maximum value V_{Lm} is 8.7 V. Furthermore, it is also verified to be in consistency with (12) that when $0° \le \sigma_Y < 90°$, i.e., the area to the left of the blue dotted line, V_L gets the peak value V_{Lp} at $\sigma_Z = \theta_Z = 0°$, and when $90° \le \sigma_Y < 180°$, i.e., the area to the right of the blue dotted line, V_L gets the peak value V_{Lp} at $\sigma_Z = \theta_Z - 180°$. However, in most cases, V_{Lp} is not equal

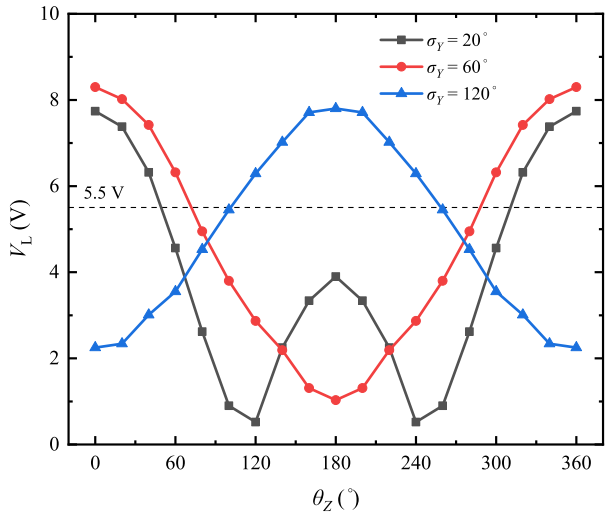

Fig. 9. V_{L} versus the change of θ_Z with fixed $\sigma_Z = 0^\circ$ under different σ_Y.

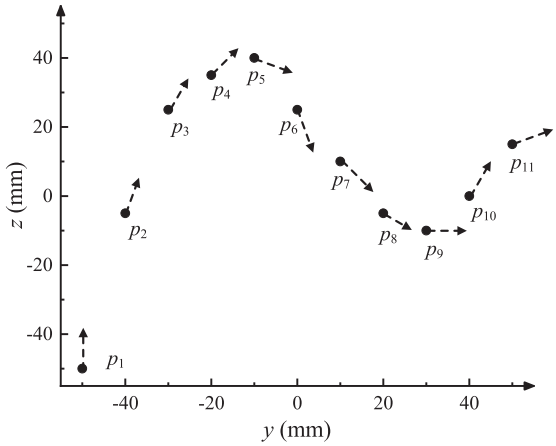

Fig. 10. Positions and attitudes of the measured points in sequence S_{a}.

to V_{Lm} except when $\sigma_Y = 45^\circ$ or 135°. For example, when σ_Y is 120°, which is marked with red dotted line, V_{Lp} can be obtained as 7.8 V. As mentioned above, the lower voltage limit is herein set to be 5.5 V, and the area in which V_{L} exceeding V_{Ls} is marked and enclosed by the black dotted line in Fig. 8(b). It reveals that even though θ_Z is unchanged, enough received voltage can cover a considerable range, which avoids continuous real-time adjustment of θ_Z.

Then, the PRC is stationary and the PTC rotates. Fig. 9 shows V_{L} versus the change of θ_Z with fixed $\sigma_Z = 0^\circ$ under different σ_Y. From the comparison, it can be obviously concluded that the peak value V_{Lp} corresponding to different σ_Y is generally not the same, and the peak value of $\sigma_Y = 120^\circ$ corresponds to the valley value of $\sigma_Y = 60^\circ$ with respect to $\theta_Z = 180^\circ$ as σ_Y are distributed in different quadrants. Moreover, it should be noted that there exists two peaks in the curve $\sigma_Y = 20^\circ$. However, though V_{L} with small σ_Y may does not vary monotonically with θ_Z, the additional peak value is extremely low and negligible compared with the primary peak value, and thus will make no difference to the mentioned strategies.

D. Test of the RVTCS

Because the positions and attitudes of the CR change continuously when it moves in the intestinal tract, it is necessary to verify the validity of the proposed RVTCS through the dynamic measurement. Due to the spatial symmetry formed by rotation, the performance in yoz plane is capable of reflecting the performance in whole 3-D space. Hence, as illustrated in Fig. 10, points $p_1 - p_{11}$ are chosen in yoz with $x = 0$, and the subscript numbers represent the time sequence in the continuous process. The three sequences, namely S_{a}, S_{b}, and S_{c} are set to have different variation modes of attitudes while the same positions. In sequence S_{a}, the attitudes are confined in yoz, i.e., with $\sigma_Z = 90^\circ$. As shown in Fig. 10, the arrows represent the attitudes of the PRC in S_{a}. Generally, S_{a} is representative of the attitudes of the CR most of the time. The extreme case is

TABLE III
POSITION AND ATTITUDE INFORMATION FOR THE MEASURED SEQUENCES

Points	Position (x, y, z)	Attitude (σ_Y, σ_Z) of S_{a}	Attitude (σ_Y, σ_Z) of S_{b}	Attitude (σ_Y, σ_Z) of S_{c}
p_1	(0,−50, −50)	(90°, 90°)	(0°, 90°)	(30°, 180°)
p_2	(0, −40, −5)	(110°, 90°)	(0°, 110°)	(60°, 150°)
p_3	(0, −30, 25)	(120°, 90°)	(0°, 120°)	(90°, 120°)
p_4	(0, −20, 35)	(135°, 90°)	(0°, 135°)	(120°, 90°)
p_5	(0, −10, 40)	(20°, 90°)	(0°, 20°)	(150°, 60°)
p_6	(0, 0, 25)	(70°, 90°)	(0°, 70°)	(180°, 30°)
p_7	(0, 10, 10)	(45°, 90°)	(0°, 45°)	(150°, 60°)
p_8	(0, 20, −5)	(30°, 90°)	(0°, 30°)	(120°, 90°)
p_9	(0, 30, −10)	(0°, 90°)	(0°, 0°)	(90°, 120°)
p_{10}	(0, 40, 0)	(120°, 90°)	(0°, 120°)	(60°, 150°)
p_{11}	(0, 50, 15)	(160°, 90°)	(0°, 160°)	(30°, 180°)

that the CR is confined in xoy plane, where the robot obtains the lowest theoretical voltage and represented as S_{b}. In addition, the sequence in which both σ_Y and σ_Z change continuously is reflected in S_{c}. Both the positions and attitudes of the three sequences are randomly changed to simulate the uncertainty in actual working conditions and cover most of the possible positions and attitudes. Table III lists the position and attitude information for the measured sequences. During the process, θ_Z of the PTC reacts under the control of the servo motor according to Fig. 6. The measured results of the three cases are presented in Fig. 11. It can be found that the measured results of V_{L} fluctuate in the range of 5.5–8.7 V regardless of the positions and attitudes, which accords with the control strategy setting. The corresponding maximum power delivered to the load (PDL) is 2523 mW with a PTE of 8.4% while the minimum PDL is 1008 mW. Noting that the overall uniformity largely depends on the control strategy setting value of the lower voltage limit V_{Ls}, a larger V_{Ls} means a better uniformity but more frequent adjustments of θ_Z. Ignoring the difference in location, the theoretical upper limit of V_{Ls} is $\frac{\sqrt{2}}{2} V_{\mathrm{Lm}}$.

The overall characteristics of the proposed 3-D omnidirectional WPT system is compared with other recently published works in Table IV. As the WPT systems for different applications differ greatly, only the systems for CR or CE application are listed. It is worth noting that the proposed work is the only one that adopts the active omnidirectional 3-D PTC, whereas other references all employ the passive 3-D PRC. Compared with

TABLE IV
COMPARISON WITH OTHER RECENTLY PUBLISHED WORKS

Reference	Omnidirectional	Dimension Number (PTC/PRC)	Coil Number (PTC/PRC)	PTC Diamter /PRC Size (mm)	Resonant Frequency (MHz)	PTE (%)	Verification of Position	Verification of Attitude
[22]	No	1-D/1-D	1/1	400/15×15	0.218	6.5	Yes	No
[20]	Yes (Passive)	1-D/3-D	1/3	400/11.5×10	0.246	4.93	Yes	No
[21]	Yes (Passive)	1-D/3-D	2/3	200/8×8	5	1.3	Yes	Yes
[32]	Yes (Passive)	1-D/3-D	1/3	690/9.5×10	0.22	3.55	No	No
[19]	Yes (Passive)	1-D/3-D	1/3	400/12.9×11.5	0.218	Not Mentioned	No	Yes
This Work	Yes (Active)	3-D/1-D	1/1	400/13×9	0.218	3.4-8.4	Yes	Yes

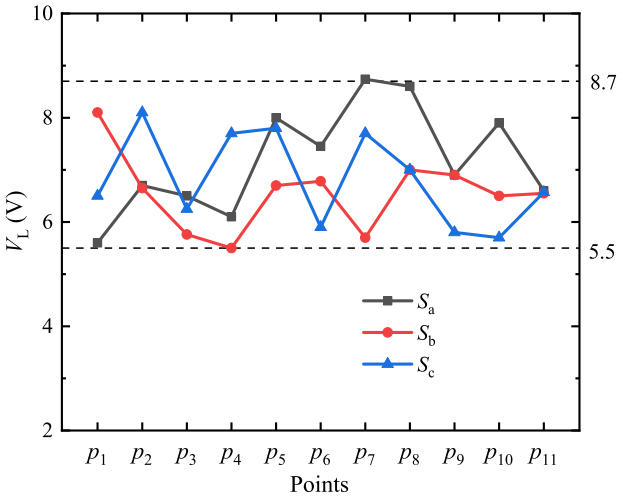

Fig. 11. Measured V_L in sequence S_a, S_b, and S_c.

the PDL ranging from 206 to 1130 mW in [18] and 485.7 to 1459.2 mW in [19] using passive 3-D PRC, the proposed active method has better uniformity. Moreover, among these methods, the proposed method requires the least number of coils.

VI. CONCLUSION

In this article, a genuine omnidirectional system for CR using only one pair of PTCs and one PRC is designed and fabricated. A single power source is utilized to drive the 1-D PTC generating 3-D omnidirectional magnetic field. Compared with the traditional topology of 3-D PRC in 1-D magnetic field, the proposed method greatly saves limited inner space of CR for more functional modules and shows better uniformity. The design parameters of the proposed compact and compatible structure are optimized through simulations and analyses. Additionally, a control strategy based on received voltage tracking is proposed to dynamically adjust the PTC rotation. Finally, the experimental results indicate the robustness to PRC positions and attitudes as well as the remarkable PTE performance.

REFERENCES

[1] Z. Luo and X. Wei, "Analysis of square and circular planar spiral coils in wireless power transfer system for electric vehicles," *IEEE Trans. Ind. Electron.*, vol. 65, no. 1, pp. 331–341, Jan. 2018.
[2] Y. Zhou, C. Liu, and Y. Huang, "Wireless power transfer for implanted medical application: A review," *Energies*, vol. 13, no. 11, Jun. 2020, Art. no. 2837.
[3] D. Kim, J. Park, H. H. Park, and S. Ahn, "Generation of magnetic propulsion force and torque for microrobot using wireless power transfer coil," *IEEE Trans. Magn.*, vol. 51, no. 11, Nov. 2015, Art. no. 8600104.
[4] Y. Lu and D. B. Ma, "Wireless power transfer system architectures for portable or implantable applications," *Energies*, vol. 9, no. 12, Dec. 2016, Art. no. 1087.
[5] D. Lin, C. Zhang, and S. R. Hui, "Mathematical analysis of omnidirectional wireless power transfer Part-I: Two-dimensional systems," *IEEE Trans. Power Electron.*, vol. 32, no. 1, pp. 625–633, Jan. 2017.
[6] D. Lin, C. Zhang, and S. R. Hui, "Mathematic analysis of omnidirectional wireless power transfer Part-II three-dimensional systems," *IEEE Trans. Power Electron.*, vol. 32, no. 1, pp. 613–624, Jan. 2017.
[7] W. M. Ng, C. Zhang, D. Lin, and S. R. Hui, "Two-and three-dimensional omnidirectional wireless power transfer," *IEEE Trans. Power Electron.*, vol. 29, no. 9, pp. 4470–4474, Sep. 2014.
[8] J. Zhao, X. Huang, and W. Wang, "Wireless power transfer with two-dimensional resonators," *IEEE Trans. Magn.*, vol. 50, no. 1, Jan. 2013, Art no. 4002804.
[9] N. X. Wang et al., "Robust 3-D wireless power transfer system based on rotating fields for multi-user charging," *IEEE Trans. Energy Convers.*, vol. 36, no. 2, pp. 693–702, Jun. 2021.
[10] Z. Ye, Y. Sun, X. Liu, P. Wang, C. Tang, and H. Tian, "Power transfer efficiency analysis for omnidirectional wireless power transfer system using three-phase-shifted drive," *Energies*, vol. 11, no. 8, Aug. 2018, Art. no. 2159.
[11] D. Wang, Y. Zhu, H. Guo, X. Zhu, T. Mo, and Q. Huang, "Enabling multi-angle wireless power transmission via magnetic resonant coupling," in *Proc. 7th Int. Conf. Comput. Convergence Technol.*, 2012, pp. 1395–1400.
[12] B. H. Choi, E. S. Lee, Y. H. Sohn, G. C. Jang, and C. T. Rim, "Six degrees of freedom mobile inductive power transfer by crossed dipole TX and RX coils," *IEEE Trans. Power Electron.*, vol. 31, no. 4, pp. 3252–3272, Apr. 2016.
[13] N. Ha-Van and C. Seo, "Analytical and experimental investigations of omnidirectional wireless power transfer using a cubic transmitter," *IEEE Trans. Ind. Electron.*, vol. 65, no. 2, pp. 1358–1366, Feb. 2018.
[14] T. Campi, S. Cruciani, F. Maradei, and M. Feliziani, "Innovative wireless charging system for implantable capsule robots," *IEEE Trans. Electromagn. Compat.*, vol. 63, no. 5, pp. 1726–1734, Oct. 2021.
[15] J. Kim, D.-H. Kim, J. Choi, K.-H. Kim, and Y.-J. Park, "Free-positioning wireless charging system for small electronic devices using a bowl-shaped transmitting coil," *IEEE Trans. Microw. Theory Techn.*, vol. 63, no. 3, pp. 791–800, Mar. 2015.
[16] R.-C. Kuo, P. Riehl, and J. Lin, "3-D wireless charging system with flexible receiver coil alignment," in *Proc. IEEE Wireless Power Transfer Conf.*, 2016, pp. 1–4.
[17] R. Carta, J. Thoné, and R. Puers, "A wireless power supply system for robotic capsular endoscopes," *Sensors Actuators A, Phys.*, vol. 162, no. 2, pp. 177–183, Aug. 2010.
[18] J. Gao, G. Yan, Z. Wang, P. Jiang, and D. Liu, "A capsule robot powered by wireless power transmission: Design of its receiving coil," *Sensors Actuators A, Phys.*, vol. 234, pp. 133–142, Oct. 2015.
[19] J. Gao et al., "Design and testing of a motor-based capsule robot powered by wireless power transmission," *IEEE/ASME Trans. Mechatronics*, vol. 21, no. 2, pp. 683–693, Apr. 2016.
[20] M. R. Basar, M. Y. Ahmad, J. Cho, and F. Ibrahim, "Stable and high-efficiency wireless power transfer system for robotic capsule using a modified helmholtz coil," *IEEE Trans. Ind. Electron.*, vol. 64, no. 2, pp. 1113–1122, Feb. 2017.
[21] S. R. Khan, S. K. Pavuluri, G. Cummins, and M. P. Desmulliez, "Miniaturized 3-D cross-type receiver for wirelessly powered capsule endoscopy," *IEEE Trans. Microw. Theory Techn.*, vol. 67, no. 5, pp. 1985–1993, May. 2019.

[22] H. Zhuang, W. Wang, K. Zhao, S. Kuang, Z. Wang, and G. Yan, "Efficient power receiving coil with novel ferrite core structure for capsule robot," *IEEE Trans. Biomed. Circuits Syst.*, vol. 16, no. 5, pp. 939–946, Oct. 2022.
[23] Y. Cheng, G. Chen, D. Xuan, G. Qian, M. Ghovanloo, and G. Wang, "Analytical modeling of small, solenoidal, and implantable coils with ferrite tube core," *IEEE Microw. Wireless Compon. Lett.*, vol. 29, no. 3, pp. 237–239, Mar. 2019.
[24] J. Gao et al., "Stable wireless power transmission for a capsule robot with randomly changing attitude," *IEEE Trans. Power Electron.*, vol. 38, no. 2, pp. 2782–2796, Feb. 2023.
[25] Y. H. Sohn, B. H. Choi, E. S. Lee, G. C. Lim, G.-H. Cho, and C. T. Rim, "General unified analyses of two-capacitor inductive power transfer systems: Equivalence of current-source ss and sp compensations," *IEEE Trans. Power Electron.*, vol. 30, no. 11, pp. 6030–6045, Nov. 2015.
[26] H. Zhuang, W. Wang, K. Zhao, Q. Fei, and G. Yan, "Design and analysis of a wireless power transfer system for capsule robot using an optimised planar square spiral transmitting coil pair," *Int. J. Med. Robot. Comput. Assist. Surg.*, vol. 18, no. 4, Aug. 2022, Art. no. e2399.
[27] F. Bonetto, E. Anoardo, and M. Polello, "Saddle coils for uniform static magnetic field generation in NMR experiments," *Concepts Magn. Reson. Part B: Magn. Reson. Eng., Educ. J.*, vol. 29, no. 1, pp. 9–19, Feb. 2006.
[28] J. Parsa and M. Mohammadzadeh, "Design and fabrication of a new multi-loop saddle coil for 1.5 T MRI," *Rev. Sci. Instrum.*, vol. 90, no. 11, Nov. 2019, Art. no. 114707.
[29] D. Ginsberg and M. J. Melchner, "Optimum geometry of saddle shaped coils for generating a uniform magnetic field," *Rev. Sci. Instrum.*, vol. 41, no. 1, pp. 122–123, 1970.
[30] Z. Jia, G. Yan, H. Liu, Z. Wang, P. Jiang, and Y. Shi, "The optimization of wireless power transmission: Design and realization," *Int. J. Med. Robot. Comput. Assist. Surg.*, vol. 8, no. 3, pp. 337–347, Sep. 2012.
[31] J. Gao et al., "Analysis of connection way of a three-dimensional receiving coil onboard a capsule robot for wireless power transmission," *Prog. Electromagn. Res. M*, vol. 78, pp. 39–48, 2019.
[32] Q. Ke, W. Luo, G. Yan, and K. Yang, "Analytical model and optimized design of power transmitting coil for inductively coupled endoscope robot," *IEEE Trans. Biomed. Eng.*, vol. 63, no. 4, pp. 694–706, Apr. 2016.
[33] Y. Meng et al., "A novel wireless power transfer system with two parallel opposed coils for gastrointestinal capsule robot," *Sensors Actuators A, Phys.*, vol. 321, Mar. 2021, Art. no. 112413.
[34] J. Zhiwei et al., "Efficiency optimization of wireless power transmission systems for active capsule endoscopes," *Physiol. Meas.*, vol. 32, no. 10, Oct. 2011, Art. no. 1561.
[35] X. L. Chen et al., "Human exposure to close-range resonant wireless power transfer systems as a function of design parameters," *IEEE Trans. Electromagn. Compat.*, vol. 56, no. 5, pp. 1027–1034, Oct. 2014.
[36] T. Campi, S. Cruciani, V. De Santis, F. Maradei, and M. Feliziani, "Near field wireless powering of deep medical implants," *Energies*, vol. 12, no. 14, Jul. 2019, Art. no. 2720.
[37] I.C. on Non-Ionizing Radiation Protection, "Guidelines for limiting exposure to electromagnetic fields (100 kHz to 300 Ghz)," *Health Phys.*, vol. 118, no. 5, pp. 483–524, May 2020.
[38] I.C. on Non-Ionizing Radiation Protection, "Guidelines for limiting exposure to time-varying electric and magnetic fields (1 Hz to 100 kHz)," *Health Phys.*, vol. 99, no. 6, pp. 818–836, 2010.
[39] T. Campi, S. Cruciani, F. Palandrani, V. De Santis, A. Hirata, and M. Feliziani, "Wireless power transfer charging system for aimds and pacemakers," *IEEE Trans. Microw. Theory Techn.*, vol. 64, no. 2, pp. 633–642, Feb. 2016.

Haoyu Zhuang was born was born in Jiangsu, China, in 1997. He received the B.S. degree in instrument science and technology from the Harbin Institute of Technology, Harbin, China, in 2019. He is currently working toward the Ph.D. degree in instrument science and technology with the Department of Instrument Science and Engineering, Shanghai Jiao Tong University, Shanghai, China.

His research interests include capsule robot, inductive wireless power transmission, and gastrointestinal biomechanics.

Wei Wang was born in Anhui Province, China, in 1992. He received the B.S. and M.S. degrees in mechanical engineering from Wuhan University of Technology, Wuhan, China, in 2012 and 2015, respectively and the Ph.D. degree in instrument science and technology from Shanghai Jiao Tong University, Shanghai, China, in 2020.

He is currently a Postdoctoral Researcher with Shanghai Jiao Tong University. His research interests include intelligent medical system, medical precision instrument, and gastrointestinal microrobot.

Guozheng Yan was born in Hunan, China, in 1961. He received the Ph.D. degree in mechanical engineering from the Jilin University of Technology, Jilin, China, in 1993.

In 1995, he became a Postdoctoral Fellow with the Nanjing University of Aeronautics and Astronautics, Jiangsu, China. He became a Professor with the Department of Instrument Science and Engineering, Shanghai Jiao Tong University, Shanghai, China, in 1997. His research interests include biomedical electronics, microsensor, microelectromechanical system, and instrument engineering.